Supporting Information

Lin et al. 10.1073/pnas.1701830114

Graphene's Surface Conductivity and BN's Permittivity

In this work, we use RPA to model the surface conductivity of graphene. RPA takes the nonlocal response into consideration (2, 27, 34), and can be fully described by the following set of equations:

$$\sigma_{s,RPA}(q,\omega) = -i\omega\chi_\tau(q,\omega) \quad \textbf{[S1a]}$$

$$\chi_\tau(q,\omega) = \frac{(1+i/\omega\tau)\chi(q,\omega+i/\tau)}{1+(i/\omega\tau)\chi(q,\omega+i/\tau)/\chi(q,0)} \quad \textbf{[S1b]}$$

$$\chi(q,\omega) = \frac{e^2}{2\pi^2\hbar q^2}\int d^2\bar{q}' \times \sum_{s,s'=\pm}\left[1+ss'\frac{\bar{q}'\cdot|\bar{q}+\bar{q}'|}{q'|\bar{q}+\bar{q}'|}\right]\frac{f_d(s'\hbar v_F|\bar{q}+\bar{q}'|)-f_d(s\hbar v_F q')}{\omega+v_F(sq'-s'|\bar{q}+\bar{q}'|)+i0^+}. \quad \textbf{[S1c]}$$

In the above, $f_d(E)=(e^{(E-\mu_c)/k_BT}+1)^{-1}$ is the Fermi–Dirac distribution function, μ_c is the chemical potential, q is the in-plane wavevector, τ is the relaxation time that characterizes the loss in graphene, the Fermi velocity $v_F=1\times10^6$ m/s, and k_B is the Boltzmann constant. When the temperature T = 0 K, we have $f_d(E)=\theta(\mu_c-E)$, where $\theta(\mu_c-E)$ is a step function. Eq. **S1c** at T = 0 K has an analytical expression

$$\chi(q,\omega) = \frac{e^2}{4\pi\hbar}\left[\frac{8k_F}{q^2v_F}+\frac{[G(-\Delta_-)-i\pi]\theta(-\Delta_--1)+G(\Delta_-)\theta(\Delta_-+1)-[G(\Delta_+)-i\pi]}{\sqrt{\omega^2-v_F^2q^2}}\right], \quad \textbf{[S1d]}$$

where $G(z)=z\sqrt{z^2-1}-\log(z+\sqrt{z^2-1})$ and $\Delta_\pm=\frac{\hbar\omega\pm2\mu_c}{\hbar v_Fq}$. The square root in $G(z)$ is chosen to yield a positive imaginary part when $|z|<1$ and is chosen to yield a positive real part when $|z|>1$ (34). The range of the imaginary part of the logarithm is chosen to be $(-\pi,\pi]$ (2, 34). In addition, we have

$$\chi(q,0) = \frac{e^2}{2\pi\hbar v_Fq}\left\{\frac{4k_F}{q}-\theta(1-x)\left[x\sqrt{1-x^2}-\cos^{-1}x\right]\right\}, \quad \textbf{[S1e]}$$

where $x=2k_F/q$. The nonlocal RPA is calculated by using these formulas in this work. Because our working frequency within BN's first reststrahlen band (~22.3–24.6 THz) is below that of the optical phonon branch of graphene, $\hbar\omega\approx0.2$ eV (~48 THz), the relaxation time of graphene can be theoretically estimated from the electron mobility (denoted as μ); i.e., $\tau=\mu_c\mu/(ev_F^2)$ (27). In this work, a conservative electron mobility of 10,000 $cm^2\cdot V^{-1}\cdot s^{-1}$ is assumed in graphene (48). In addition, because our working frequency (~22.3–24.6 THz) is much smaller than the corresponding frequency (≥36 THz) of the Fermi energy ($\mu_c\geq0.15$ eV) in this work, graphene's surface conductivities at T = 0 K and T = 300 K have trivial difference. Therefore, the temperature will have trivial influence on the phenomena of the in-plane polaritonic negative refraction demonstrated in this work.

Hexagonal BN is an anisotropic material, and its relative permittivity can be characterized by a diagonal tensor, i.e., $[\varepsilon_x,\varepsilon_y,\varepsilon_z]$, where $\varepsilon_x=\varepsilon_y\neq\varepsilon_z$. Here, we use the experimental data (11, 49) to characterize the relative permittivity of BN; i.e.,

$$\varepsilon_l(\omega) = \varepsilon_l(\infty)+s_{v,l}\frac{\omega_{v,l}^2}{\omega_{v,l}^2-i\gamma_{v,l}\omega-\omega^2}, \quad l=x,y,z. \quad \textbf{[S2]}$$

For the in-plane direction (x or y), we have $\varepsilon_l(\infty)=4.87$, the real-valued constant $s_{v,l}=1.83$ (dimensionless coupling factor), the normal frequency of vibration $\hbar\omega_{v,l}=170.1$ meV, and the amplitude decay rate $\hbar\gamma_{v,l}=0.87$ meV (11, 49). For the out-of-plane direction (z), we have $\varepsilon_l(\infty)=2.95$, $s_{v,l}=0.61$, $\hbar\omega_{v,l}=92.5$ meV, and $\hbar\gamma_{v,l}=0.25$ meV (11, 49). As discussed in ref. 11, because the nonlocal effect should appear only once q is comparable to the reciprocal lattice vector, a regime that is two orders of magnitude away from our discussed cases, it is reasonable to neglect the nonlocal effect in the permittivity of BN.

Dispersion of Hybridized Plasmon–Phonon–Polaritons

In this section, we analytically derive the formulas that govern the basic properties of hybridized plasmon–phonon–polaritons in graphene–BN heterostructures within the framework of macroscopic electromagnetic theory (50). We use the air–graphene–BN–graphene–substrate structure to illustrate our calculation method. We assume the first and second graphene layers to be located at the two interfaces (i.e., the planes of $z=0$ and $z=d$) between region 1 ($z<0$, air), region 2 ($0<z<d$, BN), and region 3 ($z>d$, substrate), where d is the thickness of the BN slab. For TM (p-polarized) waves, one can set the magnetic fields in each region (50) as

$$\bar{H}_1 = \hat{y}e^{iqx}\left(A_+e^{+ik_{1z}z}+A_-e^{-ik_{1z}z}\right) \quad \textbf{[S3a]}$$

$$\bar{H}_2 = \hat{y}e^{iqx}\left(B_+e^{+ik_{2z}z}+B_-e^{-ik_{2z}z}\right) \quad \textbf{[S3b]}$$

$$\bar{H}_3 = \hat{y}e^{iqx}\left(C_+e^{+ik_{3z}z}+C_-e^{+ik_{3z}z}\right). \quad \textbf{[S3c]}$$

The corresponding electric fields in each region can be obtained by using $(\hat{x}q+\hat{x}k_z)\times\bar{H}=-\omega\bar{\bar{\varepsilon}}\bar{E}$. In the above, $k_{z1}=\sqrt{\frac{\omega^2}{c^2}\varepsilon_{r1}-q^2}$, $k_{z2}=\sqrt{\frac{\omega^2}{c^2}\varepsilon_x-q^2\frac{\varepsilon_x}{\varepsilon_z}}$, and $k_{z3}=\sqrt{\frac{\omega^2}{c^2}\varepsilon_{r3}-q^2}$ are the wavevector components perpendicular to the interface; ε_{r1} and ε_{r3} are the relative permittivity of regions 1 and 3, respectively. The relation between parameters $A_\pm-C_\pm$ can be solved by matching the boundary conditions at the two interfaces. By letting the surface normal $\hat{n}=-\hat{z}$, we have $\hat{n}\times(\bar{E}_1-\bar{E}_2)=0$ and $\hat{n}\times(\bar{H}_1-\bar{H}_2)=\hat{x}\sigma_{s1}E_{x1}$ at $z=0$, and we have $\hat{n}\times(\bar{E}_2-\bar{E}_3)=0$ and $\hat{n}\times(\bar{H}_2-\bar{H}_3)=\hat{x}\sigma_{s2}E_{x2}$ at $z=d$. Here we denote the surface conductivity of the first and second graphene layers to be σ_{s1} and σ_{s2}, respectively.

By enforcing these boundary conditions, we obtain $\frac{C_+}{C_-}=\tilde{R}_{32}$ when the electromagnetic wave is incident from region 3; i.e.,

$$\tilde{R}_{32} = R_{32} + \frac{T_{32}R_{21}T_{23}e^{+i2k_{z2}d}}{1 - R_{21}R_{23}e^{+i2k_{z2}d}}. \quad \text{[S4]}$$

In the above, we have $R_{32} = \frac{1+\frac{\sigma_{s2}}{\omega\varepsilon_0}\frac{k_{z2}}{\varepsilon_x} - \frac{k_{z2}/\varepsilon_x}{k_{z3}/\varepsilon_{r3}}}{1+\frac{\sigma_{s2}}{\omega\varepsilon_0}\frac{k_{z2}}{\varepsilon_x} + \frac{k_{z2}/\varepsilon_x}{k_{z3}/\varepsilon_{r3}}}$, $R_{23} = \frac{1+\frac{\sigma_{s2}}{\omega\varepsilon_0}\frac{k_{z3}}{\varepsilon_{r3}} - \frac{k_{z3}/\varepsilon_{r3}}{k_{z2}/\varepsilon_x}}{1+\frac{\sigma_{s2}}{\omega\varepsilon_0}\frac{k_{z3}}{\varepsilon_{r3}} + \frac{k_{z3}/\varepsilon_{r3}}{k_{z2}/\varepsilon_x}}$, $R_{21} = \frac{1+\frac{\sigma_{s1}}{\omega\varepsilon_0}\frac{k_{z1}}{\varepsilon_{r1}} - \frac{k_{z1}/\varepsilon_{r1}}{k_{z2}/\varepsilon_x}}{1+\frac{\sigma_{s1}}{\omega\varepsilon_0}\frac{k_{z1}}{\varepsilon_{r1}} + \frac{k_{z1}/\varepsilon_{r1}}{k_{z2}/\varepsilon_x}}$, $T_{32} = \frac{2}{1+\frac{\sigma_{s2}}{\omega\varepsilon_0}\frac{k_{z2}}{\varepsilon_x} + \frac{k_{z2}/\varepsilon_x}{k_{z3}/\varepsilon_{r3}}}$, and $T_{23} = \frac{2}{1+\frac{\sigma_{s2}}{\omega\varepsilon_0}\frac{k_{z3}}{\varepsilon_{r3}} + \frac{k_{z3}/\varepsilon_{r3}}{k_{z2}/\varepsilon_x}}$, where ε_0 is the permittivity of free space.

In the main text, we denote $r_p = \tilde{R}_{32}$. Because the modes of hybridized plasmons–phonon–polaritons are the singularity poles in the coefficient of r_p, it is an instructive way to visualize the dispersion of these hybridized plasmons–phonon–polaritons via a false-color plot of $|Im(r_p)|$ as a function of q and ω (8).

When setting $\sigma_{s1} = 0$ in Eq. **S4**, one can solve the dispersion of hybridized plasmon–phonon-polaritons in the structure of air–BN–graphene–substrate. When setting $\sigma_{s1} = \sigma_{s2} = 0$ in Eq. **S4**, one can solve the dispersion of phonon polaritons in the structure of air–BN–substrate. When setting $\sigma_{s1} = 0$ and $\varepsilon_x = \varepsilon_z = \varepsilon_{r1}$ in Eq. **S4**, one can solve the dispersion of plasmon polaritons in the structure of air–graphene–substrate; i.e., $\frac{k_{z1}}{\varepsilon_{r1}} + \frac{k_{z3}}{\varepsilon_{r3}} + \frac{\sigma_{s2}}{\omega\varepsilon_0}\frac{k_{z1}}{\varepsilon_{r1}}\frac{k_{z3}}{\varepsilon_{r3}} = 0$.

Choice of the Substrate

When one selects the bulk BN to be the substrate of graphene, the mode of graphene plasmons within BN's first reststrahlen band will disappear, as shown in Fig. S1. It has been reported that a silicon (Si) substrate can locally modify the π-orbital network of the graphene layer, resulting from the covalent bonding between the carbon (C) atoms and the surface Si atoms (51). This will inevitably increase the optical losses in graphene. Due to the above facts, both bulk BN and Si are not considered as the potential substrate in this work.

To maintain the relatively low propagation loss of the highly squeezed polaritons, we consider lossless dielectrics as substrates, such as germanium (Ge) in Figs. 1 and 3 and diamond in Fig. 2. The Ge and diamond have already been widely investigated as potential substrates for graphene (35, 37, 38).

Power Flow Calculation

In addition, by setting $A_+ = C_- = 0$ in Eq. **S3** and enforcing the boundary conditions above, we can obtain the transverse electric and magnetic field distributions of the eigenmode of these ultraconfined polaritons. We can further use the transverse field distributions of these polaritonic eigenmodes to calculate their power flow in each region. Because the time-averaged Poynting's vector (power flow density) is $\langle \bar{S}(\bar{r},t)\rangle = \frac{1}{2}Re\{\bar{E}\times\bar{H}^*\}$, one can obtain the in-plane power time-averaged Poynting's vector (parallel to the x–y plane) as $\langle S_{\text{in-plane}}(\bar{r},t)\rangle = \frac{1}{2}Re\{-E_z H^*\}$. The integration of $\langle S_{\text{in-plane}}(\bar{r},t)\rangle$ with respect to z then gives the power flow of these polaritons in different regions.

In the above power flow calculation, the in-plane wavevector is assumed to be in the x direction (with $\bar{H} = \hat{y}H_y$; Eq. **S3**). Nevertheless, these formulas are applicable for cases where the in-plane wavevector is not in the x direction (with $\bar{H} = \hat{x}H_x + \hat{y}H_y$). This way, we can also use the above power flow calculation to analyze the energy flow along the y direction, such as that in Figs. 1*C*, 2*G*, and 3*G*. When the signs of the group velocity of polaritons in the left and right regions are opposite in Figs. 1*C*, 2*G*, and 3*G*, the polaritonic negative refraction will happen. This is because the power flows in the left and right regions in the y direction (parallel to the interface) are opposite. Note that the negative refraction is irrelevant to the power flow in the x direction (normal to the interface), which is always the same in the left and right regions.

Optimization of the Field Intensity in the Region of Transmission

Note that although the reflection at the discontinuous interface can affect the transmission, the field intensity of polaritons in the region of transmission also largely depends on their propagation loss. Therefore, a complete optimization of the field intensity in the region of transmission should consider both reflection and the propagation loss.

Regarding the reflection, it is widely accepted that the overlap of mode profiles can be used to estimate the reflectance qualitatively (16, 52, 53). In general, the larger the mode overlap is, the less the reflectance. However, the exact closed-form reflectance at a discontinuous interface cannot be analytically calculated with Maxwell's equations. A rough estimation of the reflectance can be done by simply extracting the effective refractive indexes (as $n = \omega/q$) and effective impedances (as $\eta = \frac{\int E_z dz}{\int H dz}$) for the incident, reflected, and transmitted polaritonic eigenmodes as plane waves, when the scattering loss at the interface is neglected. As shown in Fig. S2, the reflectance is negligible (nonnegligible) at small (large) incident angles. This is consistent with the simulation field pattern in Fig. 1*C* (or in Fig. S2, *Inset*), where interference wrinkles show up only at large angles.

To suppress the reflection, one way is to maximize the mode overlap between the incident and transmitted mode profiles at the interface (16), such as changing the BN's thickness or the chemical potential of graphene. In Fig. S3, we show that the mode overlap can indeed be increased by decreasing the BN's thickness, for the case studied in Fig. 1*C*. This indicates that the reflectance at the interface should be suppressed by using a thinner BN slab.

Practically, one needs to consider both mode overlap and polaritonic propagation loss to evaluate the quality of imaging. We implemented COMSOL simulations to discuss the impact from BN's thicknesses and chemical potentials of graphene, as shown in Fig. S4. Compared with the initial geometry (Fig. S4*A*), the field intensity in the region of transmission is not enhanced through using a thinner BN slab (Fig. S4*B*). Although the mode overlap should be enhanced with thinner BN (Fig. S3), larger propagation loss reduces the image quality in the region of transmission (Fig. S4*B*). On the other hand, increasing the chemical potential of graphene can lower the propagation loss of polaritons. Fig. S4 *A* and *C* shows that the field intensity in the region of transmission is enhanced by increasing the chemical potential of graphene, although there is still significant reflection for large incident angles in Fig. S4*C*. Note that here we assume the electron mobility in graphene, which characterizes the material loss, is constant. In practice, the increase of chemical potential might decrease the electron mobility (especially when achieved by chemical doping) and can lead to larger propagation loss of polaritons.

In summary, we find that reducing the BN thickness can improve the mode overlap (better transmission) at the cost of larger propagation loss, whereas increasing the chemical potential of graphene can reduce the propagation loss. For future experiments, optimizations should be taken into account and trade-offs should be considered for specific geometries and experimental conditions.

Negative Refraction Between Highly Squeezed Polaritons

We demonstrate an alternative structure that can enable the all-angle in-plane negative refraction between highly squeezed plasmon and phonon polaritons, as shown in Fig. S5. Different from Fig. 1, here graphene exists in both the left and right regions, which may simplify the fabrication process of the structure.

At the working frequency in Fig. 2*G* (Fig. 3*G*), there is only one polariton mode in the left region, whereas there are two (three) polariton modes in the right region in Fig. 2*G* (Fig. 3*G*), where the signs of these group velocities are different (see dispersions in Figs. 2*D* and 3*D*). When the polariton is incident from the left region in Fig. 2*G* (Fig. 3*G*), there can be double (triple) refraction at the interface, including the negative and positive refractions, making the analysis rather complicated. This indicates that the all-angle negative refraction shown in Figs. 2 and 3 is not suitable for the dipole source imaging. Therefore, to guarantee the negative refraction

only between two specific modes in the left and right regions, it is required to input the chosen polariton mode from the right region. This way, along with the phase-index–matching condition, the negative refraction between the two specific modes in the left and right regions can happen at any incident angle [i.e., (0°, 90°)] in Figs. 2*G* and 3*G*. As a demonstration of concept, the chosen polariton is incident from the right region at an angle of 45° in Fig. 2*G* and 30° in Fig. 3*G*, respectively.

In Fig. 1*C*, we demonstrate the negative refraction between graphene plasmon and the lowest-order mode of BN's phonon polariton only at 22.96 THz. However, as shown in Fig. 1*B*, the phase-index–matching point can also occur at different frequencies, between graphene plasmons and the high-order modes of BN's phonon polaritons. Therefore, the all-angle in-plane negative refraction between graphene plasmon and the higher-order mode of BN's phonon polariton is also possible. However, this in-plane negative refraction is not suitable for the dipole source imaging. Meanwhile, to guarantee the negative refraction only between two specific modes in the left and right regions, it is required to input the chosen polariton mode from the right region. The reason is the same as in the above discussion for Figs. 2*G* and 3*G*.

We also checked the refraction in the structure of air–graphene–BN–graphene–substrate (same as the right region in Fig. 2*A*), where the left and right regions have the same structure but may have different chemical potentials in graphene. It turns out that this structure is not suitable for the demonstration of the all-angle negative refraction between plasmon–polariton-like type-I hybrid polaritons. This is because for this structure, the dispersion lines of type-I hybrid polaritons with different chemical potentials in graphene do not have a phase-index–matched crossing point within BN's first reststrahlen band, as shown in Fig. S6. Note that to realize the all-angle negative refraction, the signs of the group velocity of the two type-I polaritonic modes at the crossing point should be opposite. However, there might be double or multiple refraction between type-I hybrid polaritons in this structure, among which one is the negative refraction. For example, as shown in Fig. S6, a chemical potential of 0.35 eV (0.45 eV) of graphene in the right (left) region yields two modes of type-I hybrid polaritons with different signs of the group velocity at 23.3 THz. The existence of both positive and negative dispersion will give rise to double refraction (including positive refraction and negative refraction) at 23.3 THz.

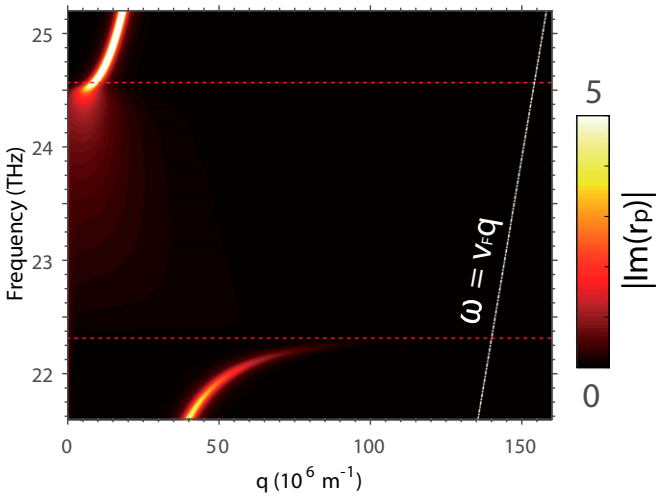

Fig. S1. Dispersion of graphene plasmons in structure of air–graphene–BN. The chemical potential of graphene is $\mu_c = 0.35$ eV.

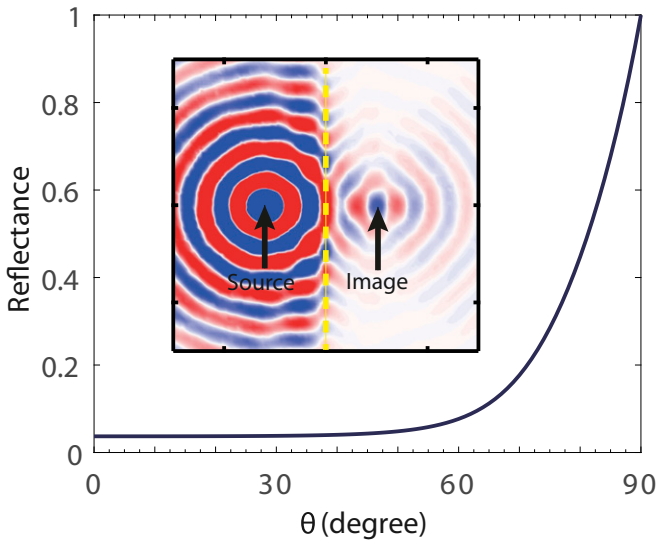

Fig. S2. Reflectance at the discontinuous interface between air–graphene–substrate and air–BN–substrate estimated from a simplified model. All setups are the same as those in Fig. 1*C*. *Inset* is from Fig. 1*C*.

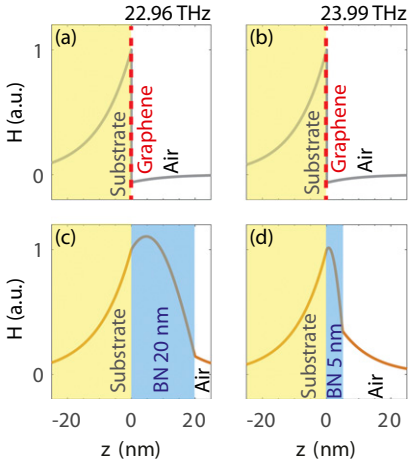

Fig. S3. Eigenmode profile of the magnetic field for (*A* and *B*) graphene plasmons and (*C* and *D*) BN's phonon polaritons at the frequency of the phase-index–matched crossing point. All parameters in *A* and *C* are the same as those in Fig. 1*C*, where the thickness of BN is 20 nm and the frequency is 22.96 THz. In *B* and *D*, the thickness of BN is decreased to 5 nm and the phase-index–matched frequency is shifted to 23.99 THz, whereas the other setups are the same as those in *A* and *C*. The mode profiles of graphene plasmons and BN's phonon polaritons are well matched only within the substrate region. The mode mismatch in the region above the substrate can be decreased by decreasing the thickness of BN.

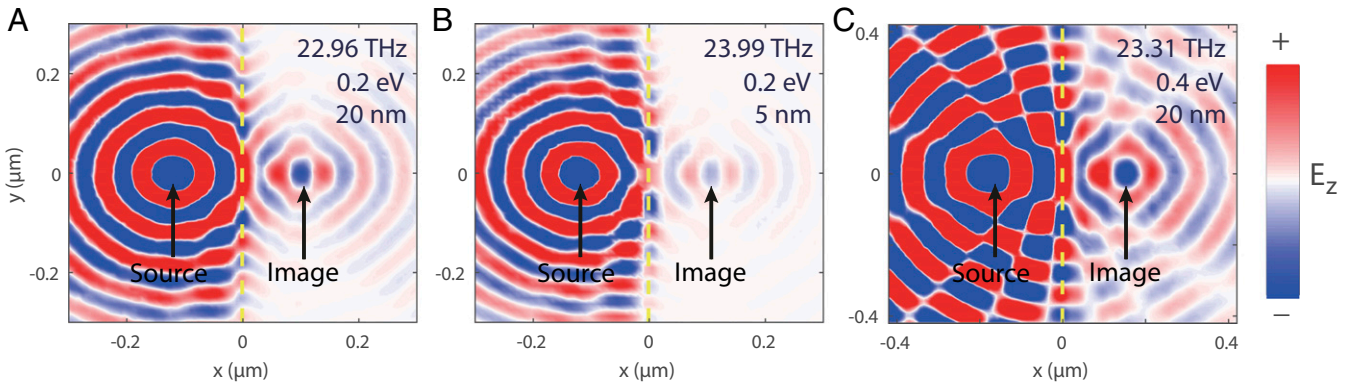

Fig. S4. All-angle negative refraction between graphene plasmons and BN's phonon polaritons at the frequency of the phase-index–matched crossing point. The frequency, the chemical potential of graphene, and the thickness of BN are denoted in each plot. (*A*) All setups are the same as those in Fig. 1*C*. The thickness of BN is 20 nm and the chemical potential of graphene is 0.2 eV. (*B*) The thickness of BN in *A* is decreased to 5 nm. (*C*) The chemical potential of graphene in *A* is increased to 0.4 eV. The wavevector $Re(q)$ is (*A*) 94×10^6 m^{-1}, (*B*) 100×10^6 m^{-1}, and (*C*) 60×10^6 m^{-1}, respectively. To compare the field intensity in the region of transmission, the distance of the dipole source from the interface (denoted as the yellow dashed line) in *C* is 94/60 times that in *A*. The ratio $|\frac{Re(q)}{Im(q)}|$, which characterizes the propagation loss, is equal to (*A*) 15, (*B*) 15, and (*C*) 47 for graphene plasmons and is equal to (*A*) 23, (*B*) 20, and (*C*) 28 for BN's phonon polaritons, respectively.

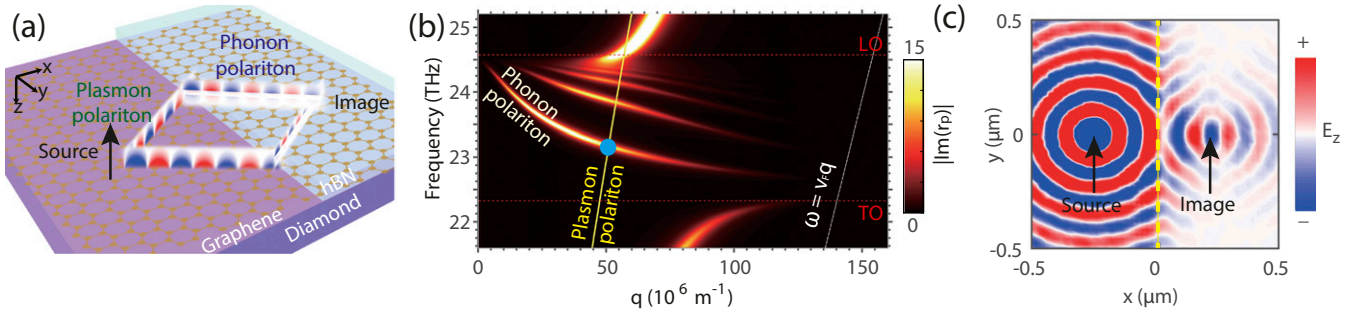

Fig. S5. In-plane negative refraction between ultraconfined graphene plasmon and phonon–polariton-like type-I hybridized polariton. (*A*) Schematic structure, along with the E_z-field distribution of plasmon and phonon polaritons. The chemical potential of graphene is $\mu_c = 0.2$ eV and the thickness of BN is 50 nm. (*B*) Dispersion of hybridized plasmon–phonon–polaritons for the right region in *A*. The yellow line is the dispersion of graphene plasmons for the left region in *A*. For the phase-index–matched blue crossing point, we have $Re(q) = 50.8\times10^6$ m^{-1} at 23.17 THz and $\frac{Re(q)}{\omega/c} = 104$; $|\frac{Re(q)}{Im(q)}|$ is equal to 23 and 15 for plasmon and phonon polaritons in the left and right regions, respectively. (*C*) E_z-field distribution excited by a dipole source at 23.17 THz.

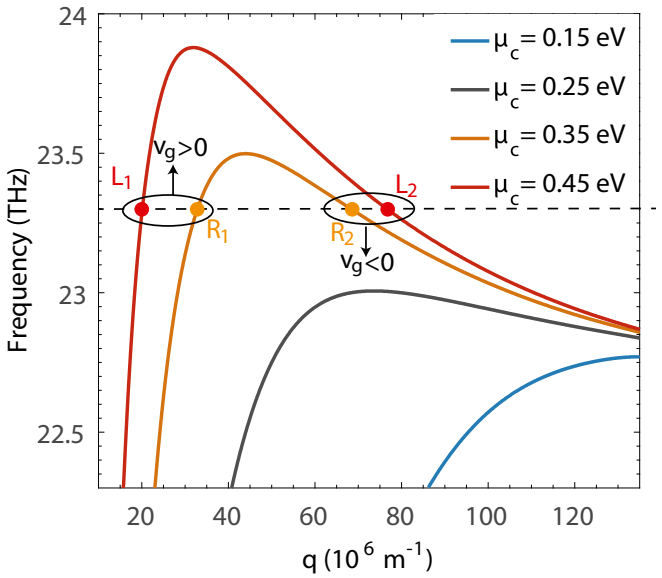

Fig. S6. Dispersion of plasmon–polariton-like type-I hybrid polaritons within BN's first reststrahlen band. The structure of air–graphene–BN–graphene–substrate is the same as that in the right region of Fig. 2*A*, where the chemical potential μ_c of graphene is labeled in the key. These four dispersion lines are extracted from the dispersion lines of type-I hybrid polaritons in Fig. 2 *B*–*E*. When $\mu_c = 0.35$ eV ($\mu_c = 0.45$ eV), there are two type-I hybrid polaritonic modes at 23.3 THz, denoted as R_1 and R_2 (L_1 and L_2), respectively. The sign of the group velocity of modes R_1 and L_1 is positive, whereas the sign of the group velocity of modes R_2 and L_2 is negative.